

Malcolm J. Andrews<sup>1</sup>

MS F644,  
Los Alamos National Laboratory,  
Los Alamos, NM 875454  
e-mail: mandrews@lanl.gov

David L. Youngs

AWE,  
Aldermaston, RG7 4PR, United Kingdom  
e-mail: david.youngs@awe.co.uk

Daniel Livescu

MS D413,  
Los Alamos National Laboratory,  
Los Alamos, NM 875454  
e-mail: Livescu@lanl.gov

Tie Wei

Department of Mechanical Engineering,  
New Mexico Tech,  
Socorro, NM 87801  
e-mail: twei@nmt.edu

# Computational Studies of Two-Dimensional Rayleigh-Taylor Driven Mixing For a Tilted-Rig

*A time-dependent, incompressible, turbulent mixing problem, referred here to as the “tilted-rig,” is defined, based results from an experiment that involved the introduction of a large-scale overturning motion, with a superposed localized Rayleigh-Taylor (RT) driven mixing. The problem serves to examine the development of RT turbulent mixing while being strained by a large-scale two-dimensional confined motion. Care is taken to define the problem in detail so others might use the definition, and the results, to help develop advanced models of buoyancy driven mixing in complex flows. Aside from a careful definition, the problem has been solved using two different implicit-large-Eddy-simulations (ILES) based codes, and with a direct numerical simulations (DNS) code. Two-dimensional and one-dimensional mix metrics are defined, and then used to examine the development of the mixing region, and the overall evolution of the flow. Comparison of simulations with experiment reveals that large-scale overturning can be well captured in all the simulations, similarly central mix widths, and spike/bubble sidewall penetrations are also in good agreement. A comparison between the different simulation methodologies, ILES and DNS, reveals an overall good agreement between mix metrics such as the amount of molecular mixing. The DNS simulations reveal a dependency on Reynolds number that merits further experimental work. [DOI: 10.1115/1.4027587]*

## 1 Introduction

The “Tilted-Rig” (T-R) test problem originates from a series of experiments (Smeeton and Youngs [1], Youngs [2]) performed at AWE in the late 1980s, that followed from the “rocket-rig” experiments (Burrows et al. [3]; Read and Youngs [4]), and exploratory experiments performed at Imperial College (Andrews [5]; Andrews and Spalding [6]). A schematic of the experiment is shown in Fig. 1, and comprises a tank filled with light fluid above heavy, and then “tilted” on one side of the apparatus. The tilt gives rise to an “angled interface” in relation to an acceleration history due to rockets attached at the top of the tank. Details of the configuration are given in the next section and include: fluids, dimensions, and other necessary details to simulate the experiment. Figure 2 shows results from two experiments, experiment 110 (which is the source for this test problem) that has an Atwood number of 0.5, and experiment 115 (a secondary source not used in this work), with Atwood of 0.9. Inspection of the photograph (the main experimental diagnostic) in Fig. 2 for experiment 110 reveals two main areas for mix development; (1) a large-scale overturning motion that produces a rising plume (spike) on the left, and falling plume (bubble) on the right, that are almost symmetric; and (2) a Rayleigh-Taylor driven central mixing region that has a large-scale rotation associated with the rising and falling plumes, but also experiences lateral strain due to stretching of the interface by the plumes, and in addition shear across the interface due to upper fluid moving downward and to the right, and lower fluid moving upward and to the left. Experiment 115 is similar but differs by a much larger Atwood of 0.9

that drives a strong asymmetry between a left side heavy spike penetration and a right side light bubble penetration. The high Atwood number is achieved by using a compressed gas/liquid combination. Moreover, the tank is heavier and accelerations are lower than for experiment 110 (which accounts for the different tank designs shown in the photographs of Fig. 2). Experiment 110 is chosen as the source for the present test problem, and investigation, because: the fluids have low surface tension (unlike experiment 115) due the addition of a surfactant; the asymmetry is small (so there is no need to have fine grids for the spike); and, there is extensive, reasonable quality, photographic data. The photographs in Fig. 2 also reveal the appearance of a boundary layer at the

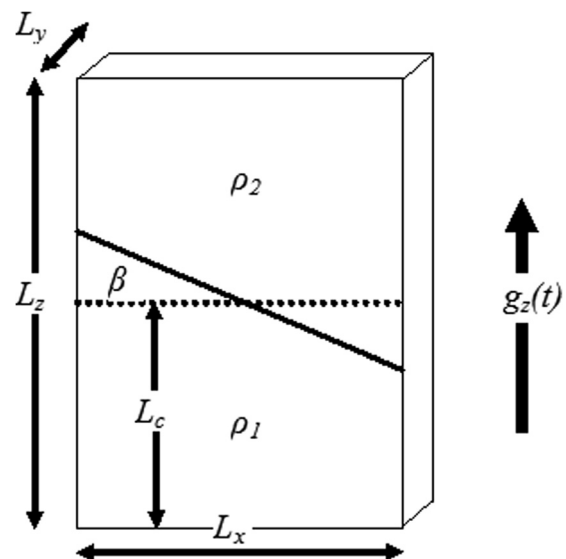
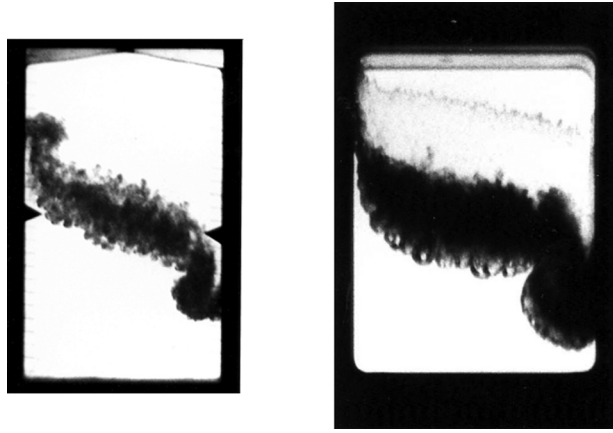


Fig. 1 Schematic of the tilted-rig experiment

<sup>1</sup>Corresponding author.

Contributed by the Fluids Engineering Division of ASME for publication in the JOURNAL OF FLUIDS ENGINEERING. Manuscript received September 12, 2013; final manuscript received April 29, 2014; published online July 9, 2014. Assoc. Editor: Dimitris Drikakis.

The United States Government retains and the publisher, by accepting the article for publication, acknowledges that the United States Government retains a non-exclusive, paid-up, irrevocable, worldwide license to publish or reproduce the published form of this work, or allow others to do so, for United States Government purposes.



**Fig. 2 Experiment 110 (a) and experiment 115 (b); British Crown Owned Copyright 2014/AWE**

left and right walls; this boundary layer has not been included in the test problem as preliminary calculations suggested it had a negligible effect on plume penetration, and the central region of RT mixing.

The significance of this test problem is that, unlike planar RT experiments such as the Rocket-Rig (Read and Youngs [4]), Linear Electric Motor (LEM) (Dimonte and Schneider [7]), or the Water Tunnel (W-T) (Snider and Andrews, [8]), the T-R is a unique two-dimensional RT mixing experiment that has experimental data and, as reported here, direct numerical simulation (DNS) data from Livescu and Wei. The goal here is to provide 3D simulation results, validated by comparison with experiments, that can be used for the development and validation of 2D Reynolds-Averaged-Navier-Stokes (RANS) models. Furthermore, the detailed comparison of simulation and experiment provides a means to study the evolution of RT mixing in a complex two-dimensional strain field. We take results from implicit-large-eddy-simulations (ILES) and DNS, and analyze them to obtain various integral quantities and 2-D sets of data that are needed for RANS model validation. The experiment is incompressible and so is directly suitable for algorithms that are designed for incompressible flows (e.g., pressure correction algorithms with multigrid); however, we have extended the numerical problem definition so that compressible algorithms, run at low Mach number, may also be used if careful consideration is given to initial pressure fields. Thus, this test problem serves as a useful tool for incompressible and compressible simulation codes, and mathematical models.

In the remainder of this manuscript, we provide a detailed specification; the next section provides the underlying

assumptions for the numerical simulations, fluids, geometry details, boundary conditions (and alternative setups), initial conditions, and acceleration history (and ways to treat the acceleration ramp at the start of the experiment). This is followed by definitions of data to be collected from the simulations. Afterwards, results are presented and discussed from the experiments, followed by simulations from Youngs using the ILES compressible TURMOIL code (Youngs [9]), Andrews using the ILES incompressible RTI3D code (Dimonte et al. [10]), and DNS from Livescu and Wei using the CFDNS code (Livescu et al. [11], and Livescu et al. [12]), We close with conclusions.

## 2 Problem Definition and Computational Details

**2.1 Geometry and Fluids.** Figure 1 is a schematic of the experimental tank giving the nomenclature for dimensions, angle definitions, and accelerations, with values given in Table 1. In experiment 110, the actual tank vertical dimension ( $L_z$ ) was 25 cm with an air bubble trap at the top of tank. We used a rectangular tank height of 24 cm to account for the air bubble trap. Preliminary simulations showed that the 2.5 cm depth ( $L_y$ ) of the tank had a negligible effect on the growth of the central RT mix zone, or the left/right plume development. However, for the purpose of collecting better statistical averages, suitable for 2D RANS model comparisons, a tank depth of 15 cm was taken (i.e.,  $6 \times$  the experimental one). The fluids used in experiment 110 were NaI solution and Hexane, and the fluid properties may be found in Table 2.

**2.2 Governing Equations.** The governing equations are:

$$\text{Mass: } \frac{D\rho}{Dt} = 0 \quad (1)$$

$$\begin{aligned} \rho \frac{Du}{Dt} &= -\frac{\partial p}{\partial x} + \nabla \cdot \mathbf{S}_u \\ \text{Momentum: } \rho \frac{Dv}{Dt} &= -\frac{\partial p}{\partial z} + \nabla \cdot \mathbf{S}_v \\ \rho \frac{Dw}{Dt} &= -\frac{\partial p}{\partial z} + \nabla \cdot \mathbf{S}_w + \rho g \end{aligned} \quad (2)$$

where  $D/Dt$  denotes the convective derivative,  $i=1$  or  $2$  for the heavy (NaI) or light (Hexane) fluids,  $\mathbf{S}_u$ ,  $\mathbf{S}_v$ , and  $\mathbf{S}_w$  are the components of the viscous stress tensor and  $g$  is the net acceleration applied to the tank. For ILES simulations described below, the viscosity is set to zero. The two fluids are immiscible in the ILES, which is modeled using a transport equation for the volume fraction of each fluid:

$$\frac{Df_i}{Dt} = 0, \quad \text{and } f_1 + f_2 = 1 \quad (3)$$

**Table 1 Geometry definitions**

Experiment	$L_x$	$L_y$	$L_z$	$\beta$ (deg)	$L_c$
110	15.0 cm	2.5 cm	24.0 cm	5 deg 46' (5.76667 deg)	12.0 cm
115	15.0 cm	5.0 cm	20.0 cm	5 deg 9' (5.15 deg)	8.3 cm

**Table 2 Fluid properties**

Experiment	Fluid	Density	Viscosity	Surface Tension	Atwood $((\rho_1 - \rho_2)/(\rho_1 + \rho_2))$
110	Fluid 1: NaI solution	1.89 g/cm <sup>3</sup>	3.3 mN s/m <sup>2</sup>	—	0.482
	Fluid 2: Hexane	0.66 g/cm <sup>3</sup>	0.31 mN s/m <sup>2</sup>		
115	Fluid 1: Pentane	0.626 g/cm <sup>3</sup>	0.23 mN s/m <sup>2</sup>	13.7 mN/m	0.903
	Fluid 2: Compressed SF <sub>6</sub>	0.0319 g/cm <sup>3</sup>			

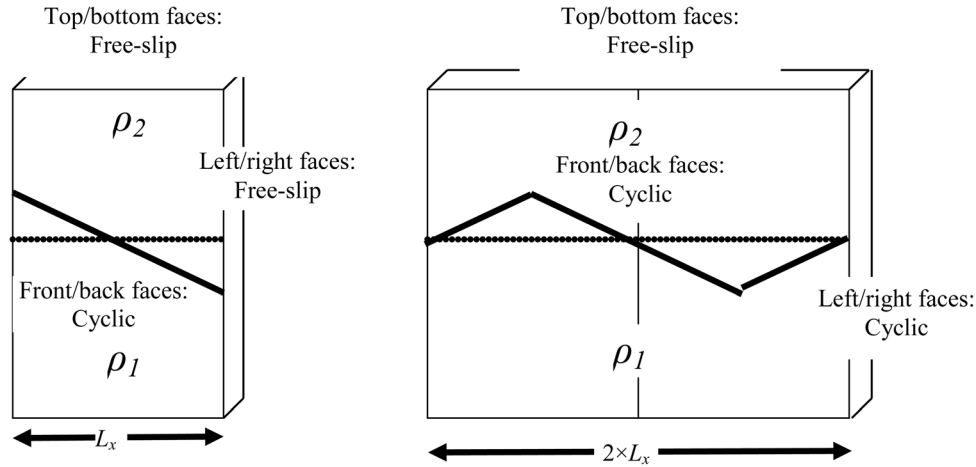


**Fig. 3** Boundary conditions; (a) is for left/right free-slip and (b) is for equivalent left/right cyclic – note saw-tooth of density interface

The CFDNS results correspond to miscible fluids for the variable density approximation (Livescu and Ristorcelli [13], Livescu et al. [11], and Wei and Livescu [14]) in which each fluid is incompressible; however, the divergence of velocity is not zero due to the change in the specific volume during mixing and depends on the mass diffusion coefficient. The specific solution method (see references above) uses high order compact finite differences coupled with Fourier transforms to ensure negligible numerical dissipation and diffusion, and relies on physical viscosity and diffusion. The Schmidt number was one in all the simulations presented here, while the kinematic viscosity (which is constant throughout the domain) was varied to study the effects of the Reynolds number. Extensive resolution studies were performed to ensure that the simulations are converged with respect to the grid size, so that all dynamically relevant scales are accurately solved and the simulations represent direct numerical simulations of this problem.

**2.3 Boundary Conditions.** We chose not to include viscous wall effects in the boundary conditions. Inspection of the experimental photographs in Fig. 2 reveals a thin boundary layer (i.e., the plume is being apparently held-back), and suggests that wall effects do have some influence. However, we do not wish to include these effects in the RANS models, and hence the 3D calculations reported later use either free-slip or cyclic boundaries to facilitate ensemble averaging for comparisons with RANS models. We specify two sets of boundary conditions (as shown in Fig. 3), as some computer simulation codes may have cyclic boundaries (e.g., spectral codes):

- (1) For codes that can specify free-slip BCs the left/right and top/bottom walls are free-slip, with the front and back as cyclic, see Fig. 3(a).
- (2) For codes that require cyclic boundary conditions on left/right boundaries, we double the width of the domain so the tilted interface becomes a complete “saw-tooth” giving left/right symmetry, the front/back walls are cyclic, and the top/bottom are free-slip; see Fig. 3(b).

**2.4 Initial Conditions.** It is known from previous research (Dimonte et al. [10], and Livescu et al. [12]) that RT simulations, with just very short wavelength perturbations, underestimate typical observed mixing rates by about a factor 2. A broadband random perturbation, with wavelengths up to half of the tank width, is used to give a mixing rate similar to that observed.

There are two main initial conditions—the density interface (to take into account the tilt and initial density perturbations) and the pressure field. For the density interface: the mean

position is specified in Fig. 3 as a solid line, with the dimensions/angles of Table 1. Interface height perturbations are superimposed as a  $P(\kappa) \sim \kappa^{-2}$  spectrum ( $\kappa = 2\pi/\lambda$ ), with  $\lambda_{\min} = 0.2$  cm,  $\lambda_{\max} = L_x/2 = 7.5$  cm, and standard deviation,  $\sigma = 0.001\lambda_{\max}$ . The power function is defined so that  $\sigma^2 = \int P(\kappa) d\kappa$  where  $\kappa = \sqrt{\kappa_x^2 + \kappa_y^2}$  is the total wavenumber for the  $x$ - $y$  plane. The random perturbation can be calculated by using the subroutine PERTINT from the IWPCTM11 web site ([http://laws.lanl.gov/IWPCTM11/TP\\_2\\_pertint.txt](http://laws.lanl.gov/IWPCTM11/TP_2_pertint.txt)). In that case the input required is  $SS = -2.0$ ,  $XLMIN = 0.2$ ,  $XLMAX = 7.5$ ,  $SD = 0.0075$ . The interface height (tilt + perturbation) defines the fluid volume fractions,  $f_1, f_2$ , for each cell and hence the initial density:  $\rho = f_1\rho_1 + f_2\rho_2$ ; alternatively, for DNS one would use the same PERTINT routine but initialize the density perturbations through an error function (Wei and Livescu [14]), to ensure the smoothness of the profile so that it can be resolved on the specific grid used.

Initial velocity fields are set to zero. For RTI3D incompressible and CFDNS simulations the initial pressure field is set up by the Poisson solver during the first time step, and the imposed rocket acceleration is time varying with the measured time history of the acceleration,  $g$ , given in Table 3. However, a time-varying acceleration  $g(t)$  is not recommended here for compressible simulations to avoid a global adjustment to the pressure field needed throughout the simulation. For compressible simulations a suitable constant acceleration,  $\bar{g}$ , should be used rather than the time-varying one  $g(t)$ , and we also recommend a suitable Poisson equation should be solved for the initial pressure field. In particular, for compressible simulations the initial pressure field should be found (as for incompressible simulations) by solving the Poisson equation:

$$\nabla \cdot \left( \frac{1}{\rho} \nabla p \right) = 0 \text{ with } \frac{\partial p}{\partial x} = \rho g \text{ at the upper and lower boundaries} \quad (4)$$

The influence of compressibility is reduced if an adiabatic variation is assumed within each fluid (i.e., neutral stability within each fluid). This can be incorporated into the Poisson equation as proposed by Holford et al. [15]. Let  $\rho_0 = f_1\rho_1 + f_2\rho_2$  denote the density which would be used in an incompressible simulation. Then for the adiabatic variation the pressure is given by:

$$\frac{p}{p_0} = \left( \frac{\rho}{\rho_0} \right)^\gamma \text{ with } p_0 = \text{initial interface pressure and } \gamma = \frac{5}{3} \quad (5)$$

**Table 3 Acceleration history**

Experiment 110	
#	RT110 acceleration versus time
#	adjusted to match measured tank distance versus time
#	assumes linear interpolation between data points
#	$g$ = gravity to be used RT simulations
#	tank acceleration = $g+g_0$ (acceleration used to calculate tank distance)
#	$g_0 = 0.00980665$ mm/ms <sup>2</sup> : gravitational acceleration
#	t(ms) acceleration(g/g <sub>0</sub> )
0.0	0.000
2.0	0.000
3.0	1.018
4.0	3.258
5.0	6.515
6.0	10.180
7.0	14.150
8.0	18.019
9.0	21.582
10.0	24.636
11.0	26.875
12.0	28.809
13.0	30.540
14.0	32.067
15.0	33.187
16.0	34.103
17.0	34.816
18.0	35.426
19.0	35.732
20.0	36.037
21.0	36.343
22.0	36.444
23.0	36.546
24.0	36.750
25.0	36.648
80.0	34.510
81.0	34.307
82.0	34.103
83.0	33.289
84.0	32.169
85.0	30.744

The Poisson equation can then be written in the form:

$$\nabla \cdot \left( \frac{1}{\rho_0} \nabla p^* \right) = 0 \text{ with } p^* = \frac{\gamma}{\gamma-1} p_0^{\frac{1}{\gamma}} p^{\frac{\gamma-1}{\gamma}} \text{ and } \frac{\partial p^*}{\partial x} = \rho_0 g \text{ at the upper and lower boundaries} \quad (6)$$

A standard Poisson solver may then be used to find the initial pressure field. If gm-cm-ms units are chosen then the unit for pressure is the bar. In the present work the recommended interface pressure for compressible simulations is  $p_0 = 20$  bar. This gives a peak Mach number of  $\sim 0.25$  and increasing the pressure should have little effect.

Section 2.5 describes the evaluation of the constant acceleration.

**2.5 Acceleration History and Simulation Time Scale.** The tank acceleration for experiment 110 ramped-up during the initial motion, with measured accelerations given in Table 3, and plotted in Fig. 4. We note from Table 3 that the acceleration attained a roughly constant value after 12 ms. There are two ways to represent the variable acceleration: (1) incorporate Table 3 directly into the simulation (i.e., a variable “ $g$ ”), however this may create problems for compressible codes; or, (2) make use of a constant acceleration. For simulations that use a constant acceleration, a nondimensional time,  $\tau$ , is used for comparison with experimental results and with variable  $g(t)$  simulations, and a suitable time is given by:

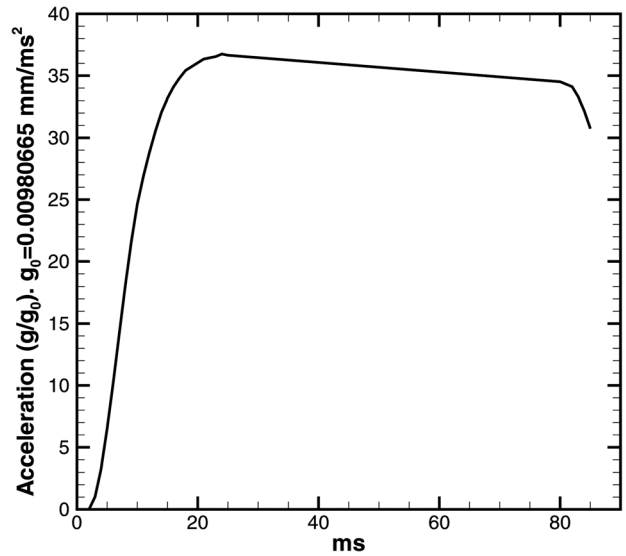


**Fig. 4 Acceleration history for experiment 110**

$$\tau = \int \sqrt{\frac{Ag}{L_x}} dt + \delta \quad (7)$$

where  $\delta$  is a correction term described below.

To obtain a suitable equivalent constant  $\bar{g}$  we consider the influence of the variable acceleration on a single mode RT growth (wavelength  $\lambda$ ), which may be found by combining Layzer’s [16] equation for bubble growth at  $A_t = 1$  with Goncharov’s [17] limiting bubble and spike velocities,  $V_{b,s}$ , for arbitrary  $A$  determined from:

$$V_{b,s} = \frac{dh}{dt} \text{ and } (2 + E) \frac{dV_{b,s}}{dt} = (1 - E)Ag - \frac{C_{D_{b,s}} V_{b,s}^2}{\lambda} \quad (8)$$

where  $E = \exp(-6\pi/\lambda)$  and  $C_{D_{b,s}} = \begin{cases} 3\pi(1 + A) & \text{bubble} \\ 3\pi(1 - A) & \text{spike} \end{cases}$

The model is approximate but the derivation does not assume that  $g$  is constant. The above equations are solved for constant  $g$ , and then again using the experimental acceleration history, with values of  $\lambda$  typical of the large scale overturning motion. Results are shown in Fig. 5 for experiment 110 with  $\lambda = L_x$  and  $h_0 = (1/2)L_x \tan \theta$ . The bubble and spike distances are plotted in Fig. 5 against the nondimensional time,  $\tau$ , defined Eq. (7). If the correction  $\delta = -0.053$  is used the  $g(t)$  results overlay the constant  $\bar{g}$  results, and provide a constant acceleration value of  $\bar{g} = 0.035$  cm/ms<sup>2</sup>.

**2.6 Computational Grids and Time Steps.** For the tank cross section we have taken the physical width as  $L_x = 15$  cm, the depth  $L_y = 15$  cm (6  $\times$  the physical depth as described above), and the vertical height  $L_z = 24$  cm. These dimensions are the reference case for all the results reported below; most of the results were unaffected by the upper and lower boundaries with increasing  $L_z$ , but a larger value should facilitate the use of powers of 2 for the grid sizes. Next, we discuss the grids used with the three codes, and we note that at least two different mesh sizes should be used to examine mesh convergence.

Computational grid for TURMOIL simulations (Yongs):

- (a)  $L_x = L_y = 15$  cm,  $L_z = 24$  cm;  $300 \times 300 \times 480$  ( $N_x \times N_y \times N_z$ )
- (b)  $L_x = L_y = 15$  cm,  $L_z = 60$  cm;  $300 \times 300 \times 1200$  ( $N_x \times N_y \times N_z$ )

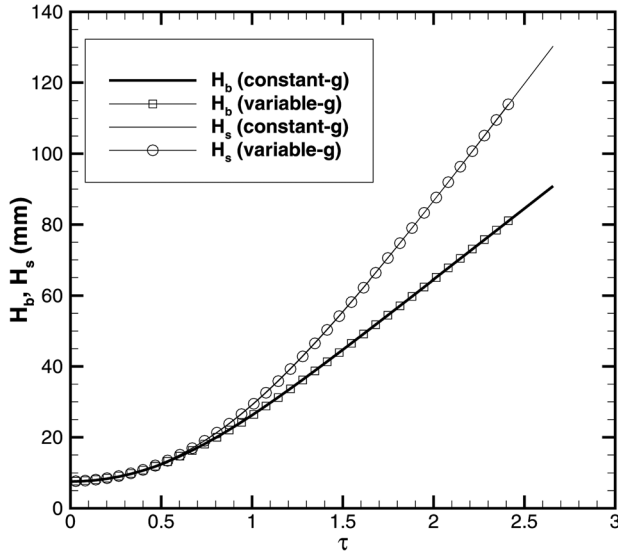


Fig. 5 Layer equation model: bubble and spike distances for experiment 110

- (c)  $L_x = L_y = 15$  cm,  $L_z = 24$  cm;  $600 \times 600 \times 600$  ( $N_x \times N_y \times N_z$ )  
 (d)  $L_x = L_y = 15$  cm,  $L_z = 24$  cm;  $600 \times 600 \times 960$  ( $N_x \times N_y \times N_z$ ), no tilt.

Comparison of (a) and (b) shows the influence of the upper and lower boundaries. For b) the upper and lower boundaries should reveal little effect during the entire simulation. Comparison of (a) and (c) shows the effect mesh resolution. Calculation (d) shows how much mixing occurs if the tilt is not present.

Computational grid for the RTI3D simulations (Andrews):  
 with  $(\Delta x) \times (\Delta y) \times (\Delta z) = (L_x/N_x) \times (L_y/N_y) \times (L_z/N_z)$ :

- (a)  $L_x = L_y = 15$  cm,  $L_z = 24$  cm;  $320 \times 320 \times 480$  ( $N_x \times N_y \times N_z$ )  
 (b)  $L_x = L_y = 15$  cm,  $L_z = 24$  cm;  $512 \times 512 \times 768$  ( $N_x \times N_y \times N_z$ )

The intent was to keep cell sizes similar, while maintaining a power of 2 suitable for a multigrid pressure algorithm with up to four levels of refinement. The choice of time step was automatic according to an accuracy or stability condition, and it was that a time step of  $2 \times 10^{-6}$  s gives a maximum Courant number during the simulation of about 0.2.

Computational grid for the CFDNS simulations (Livescu and Wei):

The DNS runs presented here were obtained for three grid sizes corresponding to the domain:

$L_x = L_y = 15.0$  cm,  $L_z = 24$  cm; and to the following perturbation Reynolds numbers ( $Re_p = \lambda_{\max}(Ag\lambda_{\max}/(A+1))^{1/2}/\nu$ ):

$$Re_p = 14000: 1536 \times 1536 \times 3072 (N_x \times N_y \times N_z)$$

$$Re_p = 7500: 1024 \times 1024 \times 2048 (N_x \times N_y \times N_z)$$

$$Re_p = 2500: 512 \times 512 \times 768 (N_x \times N_y \times N_z)$$

The grid spacing is finer in the vertical direction, which is necessary to ensure the required accuracy of the numerical approach (Livescu et al. [11], Wei and Livescu [14]). For all Reynolds number values, the results are converged under mesh refinement, and the simulations solve all dynamically relevant scales of motion. The Reynolds number is varied by changing the fluid viscosity. The viscosity used for the highest  $Re_p$  case is about ten times larger than the experimental value. As shown by Wei and Livescu

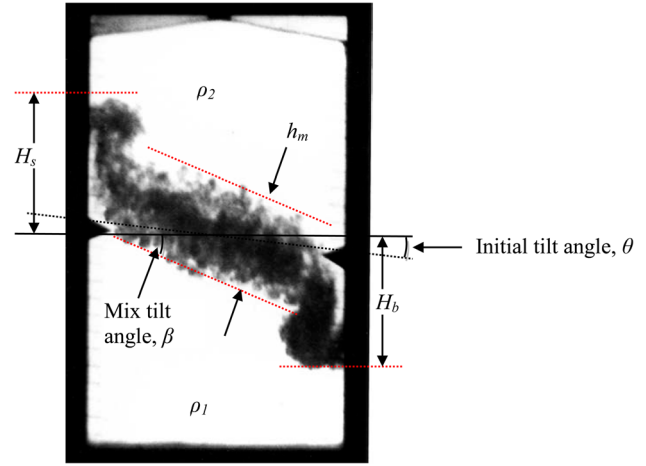


Fig. 6 Definition of measurement quantities:  $H_s$ ,  $H_b$ ,  $h_m$ ,  $\beta$ ,  $t_{\text{exp}} = 45.3$  ms,  $\tau = 1.256$   $t_{\text{exp}} = 59.8$  ms,  $\tau = 1.741$   $t_{\text{exp}} = 71.1$  ms, and  $\tau = 2.117$

[14], there is a clear distinction in the single mode RTI development at high and low Reynolds numbers, and single mode RTI will grow quadratically in time at high enough values of  $Re_p$ . This is different than the “terminal bubble velocity” assumed to be attained at late times in previous studies, and implicit in the Layer model of Eq. (8). The threshold for this change in behavior seems to occur at around  $Re_p \sim 10000$ . The three Reynolds numbers chosen correspond to a low value and two other values, one slightly below, and the other above this threshold. Since the wall bubble and spike have many similarities with single mode RTI, it is important to specify a high enough  $Re_p$  value to demonstrate the high Reynolds number asymptotic behavior of the results.

The results are also sensitive to the initial perturbation variance and differences in the mixing parameters are expected when compared with the Turmoil and RTI3D simulations, as the initial density fields are different. Thus, even though the initial perturbation is generated following the same procedure, the CFDNS density field is constructed by passing the initial perturbation through an error function profile.

### 3 Definitions of Data Collected From the Simulations

**3.1 Integral Values to be Plotted Versus Nondimensional Time,  $\tau$ .** Let  $\bar{\phi}(x, z)$  denote the average of  $\phi$  in the y-direction and let  $\bar{\phi}(z)$  denote the average of  $\phi$  over an x-y plane. The following integral quantities have been computed as functions of time for the calculations with and without the tilt-angle included (except for the mix tilt-angle):

- (1) Left (spike) and right (bubble) plume penetration ( $H_s$  and  $H_b$ ), see Fig. 6. For the calculations with the tilt included, these are measured to the points where  $\bar{f}_1 = 0.001$  and  $\bar{f}_2 = 0.001$ . For the calculations without the tilt included, these are measured to the points where  $\bar{f}_1 = 0.01$  and  $\bar{f}_2 = 0.01$ .
- (2) Mix tilt-angle,  $\beta$  (see Fig. 6). This is derived from the mean interface height calculated as a function of x:

$$h(x) = \int_{z_{\min}}^{z_{\max}} \bar{f}_1(x, z) dz \quad (9)$$

The tilt-angle (in degrees) is then found from a least-squares linear fit to the values of  $h(x)$  for central 40% of the x-range. This formula should give a good estimate up to stage 2 (Sec. 3.1.2). The side bubble and spike will affect the results at later stages.

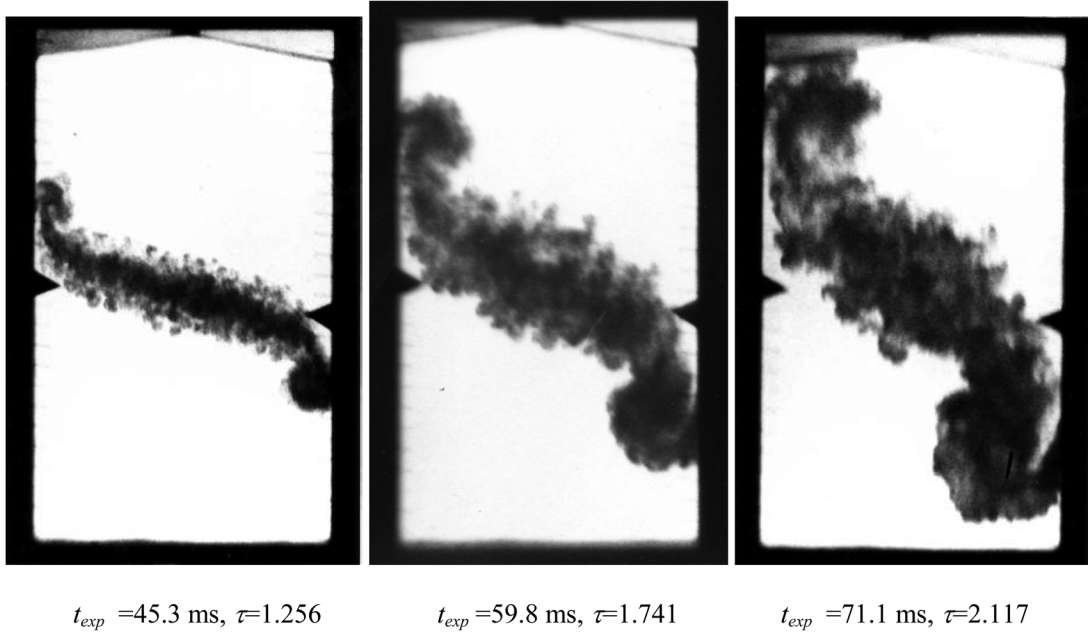


Fig. 7 Experiment 110. Stages selected for comparison with numerical simulations

(3) Integral mix width. For calculations with and without the tilt, this is defined as (Spalding and Andrews, [6]):

$$W = \int \bar{f}_1 \bar{f}_2 dx dz / L_x \quad (10)$$

(for the calculation without the tilt this should be close to  $\bar{W} = \int \bar{f}_1 \bar{f}_2 dz$ ).

Table 4 Equivalent times at which the photographs of Figure were taken

Photographs	$\tau$	$t_{exp}$	$t_{\bar{g}}$
1	1.256	45.3	37.43
2	1.741	59.8	51.90
3	2.117	71.1	63.11

(4) Total turbulence kinetic energy,  $k_{TOT}$ . This is defined as follows.

The total kinetic energy is:  $K = \frac{1}{2} \int \rho u^2 dx dy dz = \tilde{K} + k_{TOT}$

where  $\tilde{K} = \frac{1}{2} L_y \int \bar{\rho} (\bar{u}_x^2 + \bar{u}_z^2) dx dz$  is the mean flow

kinetic energy, and  $k_{TOT} = L_y \int \bar{\rho} k dx dz$ ,

$$\text{with } k = \frac{1}{2} \frac{\rho \left\{ (u_x - \bar{u}_x)^2 + u_y^2 + (u_z - \bar{u}_z)^2 \right\}}{\bar{\rho}},$$

$$\bar{u}_x = \frac{\rho \bar{u}_x}{\bar{\rho}}, \quad \bar{u}_z = \frac{\rho \bar{u}_z}{\bar{\rho}} \quad (11)$$

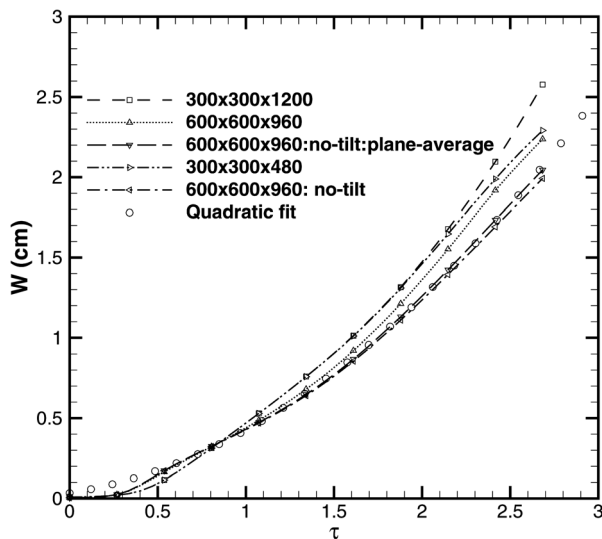


Fig. 8 TURMOIL integral mix widths of Eq. (10)

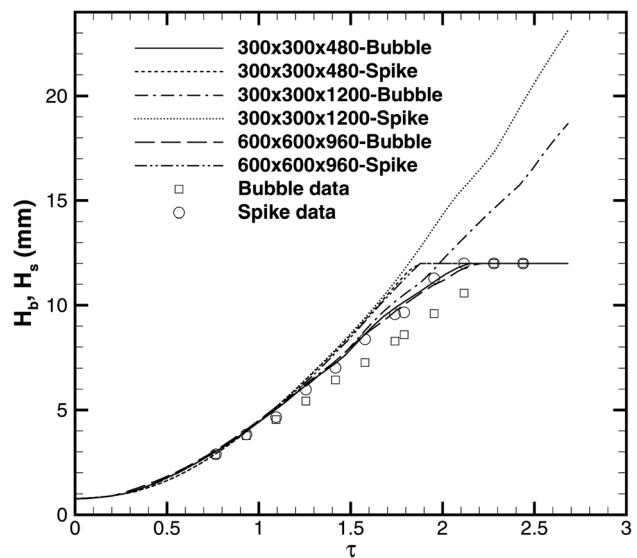


Fig. 9 TURMOIL sidewall bubble and spike positions,  $H_b, H_s$  versus  $\tau$

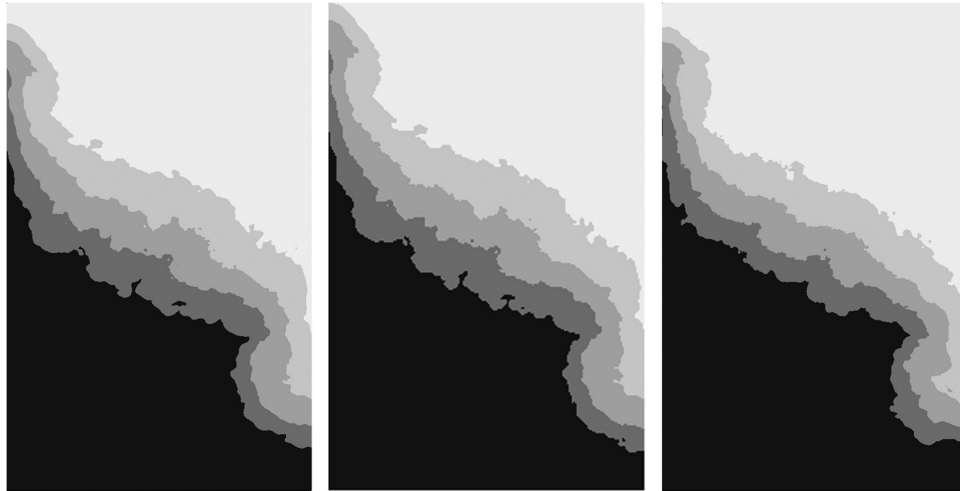


Fig. 10 TURMOIL volume fraction distributions at  $\tau = 1.741$ : (a)  $300 \times 300 \times 480$  meshes, (b)  $300 \times 300 \times 1200$  meshes (clipped image), and (c)  $600 \times 600 \times 960$  meshes. Contour levels 0.025, 0.3, 0.7, and 0.975.

(5) Global molecular mixing parameter is defined as:

$$\Theta = \frac{\int \bar{f}_1 \bar{f}_2 dx dz}{\int \bar{f}_1 \bar{f}_2 dx dz} \quad (12)$$

(6) Energy dissipation fraction is defined as:

$$\Delta = \frac{D}{D + k_{TOT}} \quad (13)$$

where  $D$  is the total KE dissipation, and may be calculated from the viscous or sub-grid LES dissipation (or if the change in internal energy is negligible and energy

conservation is good, from the relation  $P = D + K$  where  $P$  is the loss of potential energy).

### 3.2 Two-Dimensional Data Plots at Selected Times.

We have chosen to study the simulation results at three times that correspond to experimental photographs, namely  $t_{exp} = 45.3$  ms, 59.8 ms and 71.1 ms (we note that  $t_{exp} = 59.8$  ms is the last experimental time for which the results are unaffected by the upper and lower bound boundaries). The experimental photographs are shown in Fig. 7. Inspection of the photographs suggests that  $t_{exp} = 45.3$  ms corresponds to the time when the amount of mixing is about half that at the time of  $t_{exp} = 59.8$  ms. Table 4 gives the values of  $\tau$  that are being considered and the equivalent constant  $\bar{g}$  times ( $t_g$ ).

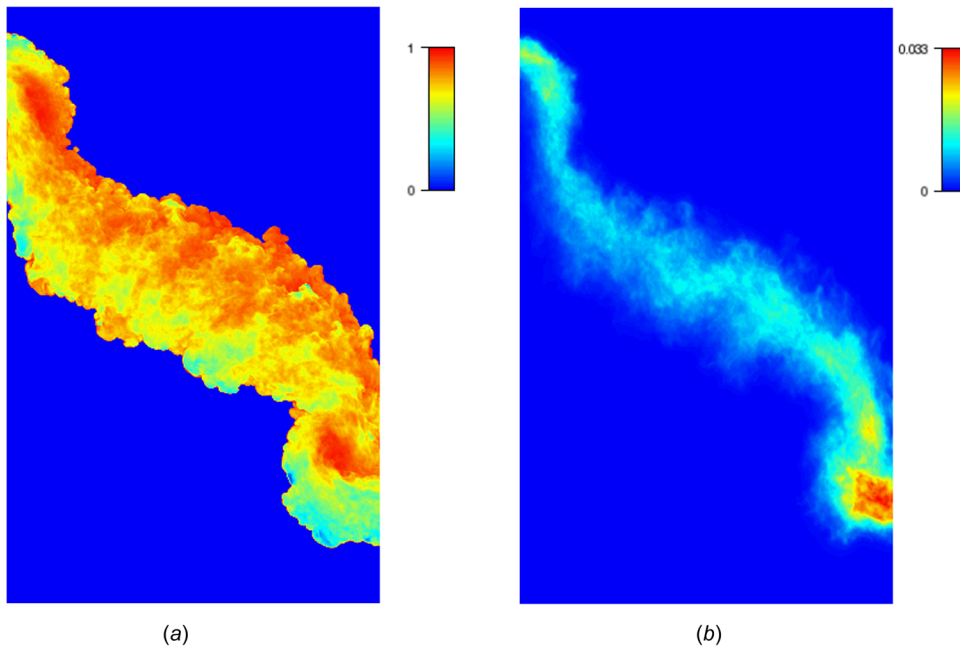


Fig. 11 TURMOIL results for  $600 \times 600 \times 960$  meshes at  $\tau = 1.741$ . (a) molecular mixing parameter,  $\theta$  and (b) turbulence kinetic energy,  $k$ , scale maximum =  $0.033 \text{ cm}^2/\text{ms}^2$

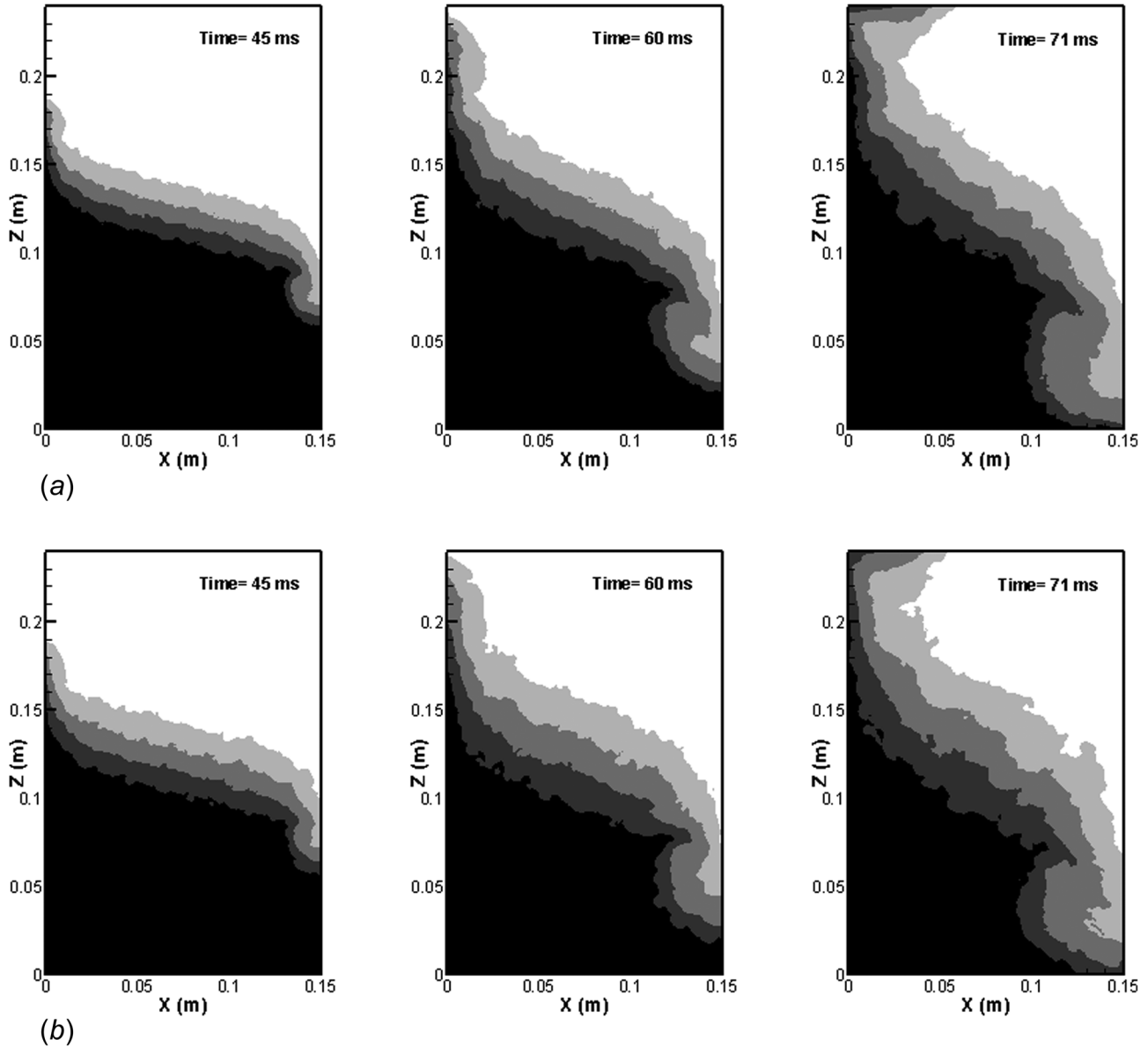


Fig. 12 (a) RTI3D volume fraction distributions at 45 ms, 60 ms, and 71 ms using a  $512 \times 512 \times 768$  mesh with contour levels of 0.025, 0.3, 0.7, 0.975. (b) RTI3D volume fraction distributions at 45 ms, 60 ms, and 71 ms using a  $320 \times 320 \times 480$  mesh with contour levels of 0.025, 0.3, 0.7, 0.975.

For calculations with the tilt-angle included, the following 2D plots of  $y$ -averaged quantities have been considered:

- (1) Fluid 1 volume fraction,  $\bar{f}_1$ , (contour values, 0.025, 0.3, 0.7, 0.975).
- (2) Turbulence kinetic energy,  $k$ , as defined in Eq. (11).
- (3) Dissipation rate per unit mass,  $\varepsilon$ , defined by (this quantity can be derived for TURMOIL from the remap step in the algorithm, but is not readily available for ILES simulations of RTI3D):

$$\varepsilon(x, z) = \frac{\int (\text{dissipation rate per unit volume}) dy}{\int \rho dy} \quad (14)$$

- (4) Molecular mixing parameter:

$$\theta(x, z) = \frac{\bar{f}_1 \bar{f}_2}{\bar{f}_1 \bar{f}_2} \quad (15)$$

- (5) The BHR (Livescu et al. [11])  $b$ -parameter:

$$b(x, z) = \overline{\rho'v'} \quad (16)$$

where  $v = l/\rho$  and the primes denote fluctuations  $\phi' = \phi - \bar{\phi}$

- (6) Mass fluxes in horizontal and vertical directions:

$$a_x = \frac{\overline{\rho'u'_x}}{\bar{\rho}}, \quad a_z = \frac{\overline{\rho'u'_z}}{\bar{\rho}} \quad (17)$$

## 4 Results

**4.1 Results From TURMOIL.** Results for the TURMOIL simulations listed in Sec. 2.4.3 are shown in Figs. 8–11. Figure 8 shows a plot of  $\bar{W} = \int \bar{f}_1 \bar{f}_2 dz$  versus  $\tau$  for the simulation without tilt. The data points (excluding the early time values) are fitted by the curve:

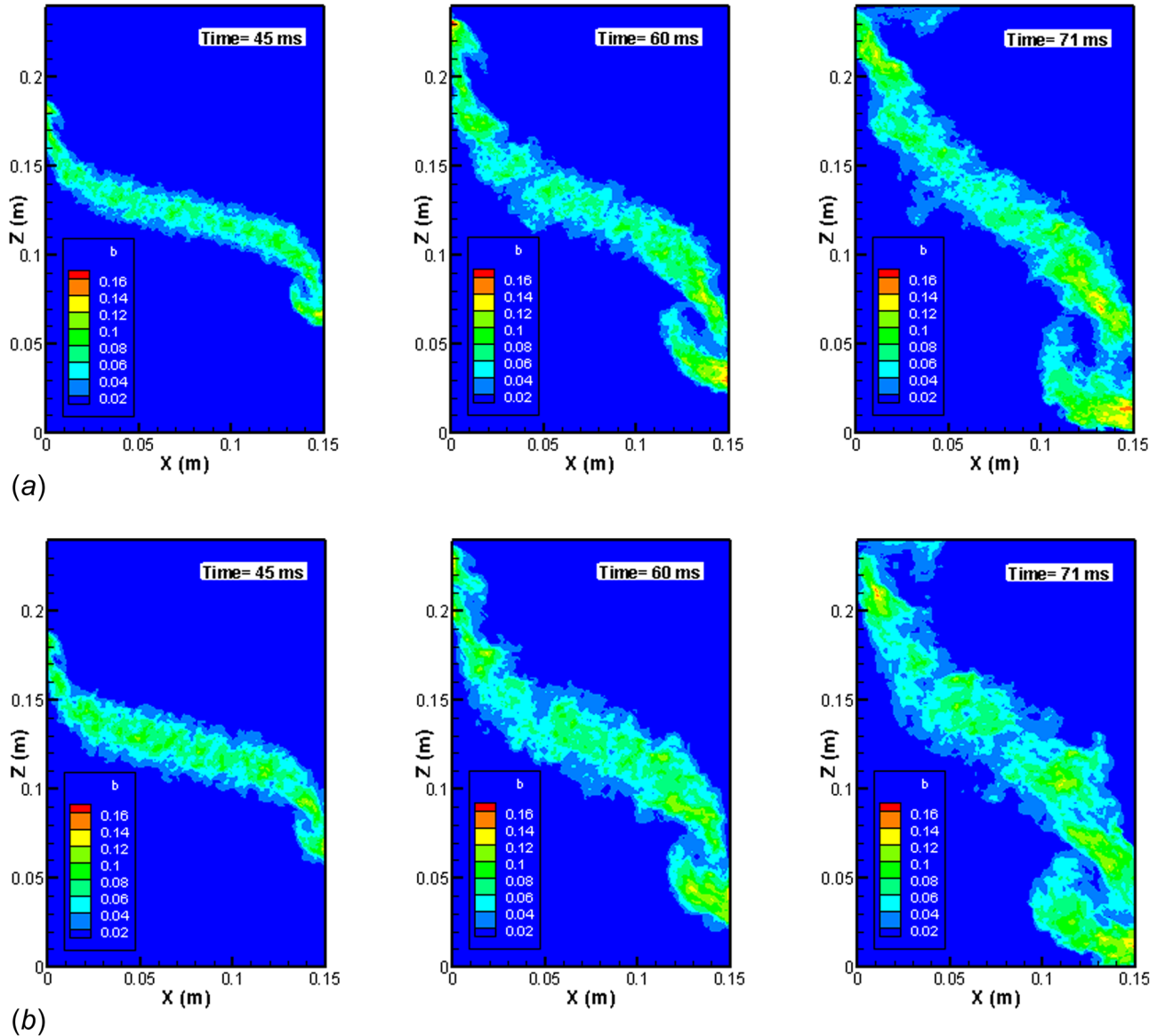


Fig. 13 (a) RTI3D “*b*” distributions at  $t = 45$  ms, 60 ms and 71 ms using a  $512 \times 512 \times 768$  mesh and (b) RTI3D “*b*” distributions at  $t = 45$  ms, 60 ms and 71 ms using a  $320 \times 320 \times 480$  mesh

$$h_b = 3.3 \bar{W} = \alpha L_x (\tau + \tau_0)^2 \quad (18)$$

where  $\tau_0$  represents a time-offset (Snider and Andrews, [8]). This gives  $\alpha = 0.048$  and quantifies the influence of initial conditions on the problem without tilt. When the tilt is included the amount of mixing, as measured by  $W = \int \bar{f}_1 \bar{f}_2 dx dz / L_x$ , is increased slightly. Mesh resolution has some effect. The coarser mesh gives slightly more mixing. This is attributed to the reduced dissipation of density and velocity fluctuations at early time when the turbulence is poorly resolved.

Figure 9 shows that the calculated values of  $H_b$  and  $H_s$  are insensitive to the mesh resolution and are little affected by the upper and lower boundaries until the side bubble/spike gets very close to the boundaries. This is confirmed by the contour plots shown in Figs. 10(a) and 10(b). Figures 10(a) and 10(c) show similar volume fraction distributions at the two mesh resolutions. However, at the higher mesh resolution, the central mixing zone is somewhat thinner (as expected from Fig. 8). The experimental values of  $H_b$  and  $H_s$  are somewhat less than the calculated values (Fig. 9). Moreover, the bubble and spike at the sides of the tank in the experiment tend to pull away from the walls. This difference

in behavior is attributed to the influence of the wall boundary layers.

Figure 11 shows contour plots for  $\theta$ , the molecular mixing parameter, and  $k$ , the turbulence kinetic energy at  $\tau = 1.741$ . Note that in the central region  $\theta$  is higher on the spike side of the mixing zone than the bubble side. This is attributed to the higher velocity fluctuations on the spike side.

**4.2 Results From RTI3D.** Figures 12 through 15 show results from RTI3D simulations listed above in Sec. 2.6. Units are meters (m), seconds (s), and kilograms (kg). Comparison of the RTI3D results in Fig. 12(a), particularly the middle 60 ms ( $\tau = 1.7410$ ) and  $512 \times 512 \times 768$  mesh, with the closest corresponding results of TURMOIL in Fig. 10(c),  $600 \times 600 \times 900$  mesh, reveals good agreement. In particular, we note the close agreement of bubble and spike penetration and shape. Moreover, the centerline mix width shows a reasonable comparison, with the TURMOIL mix width slightly wider than that from RTI3D. Just like TURMOIL, we note that comparison of the RTI3D  $512 \times 512 \times 768$  mesh results in Fig. 12(a), with the RTI3D  $320 \times 320 \times 480$  mesh results in Fig. 12(b) reveals a good match

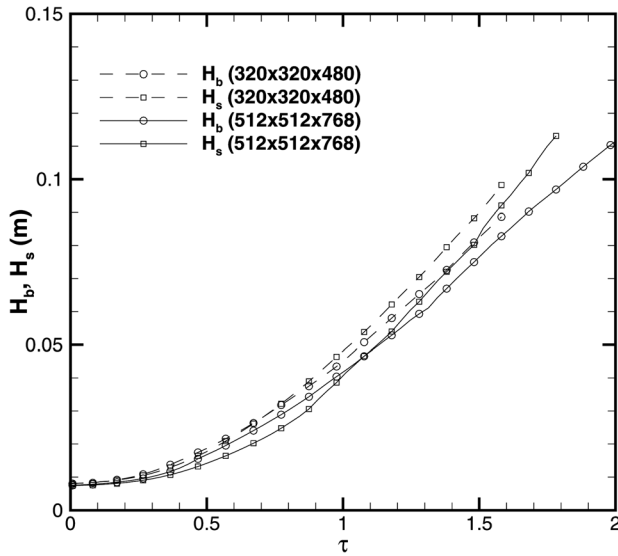


Fig. 14 RTI3D sidewall bubble and spike positions,  $H_b$ ,  $H_s$  versus  $\tau$  for  $320 \times 320 \times 480$  and  $512 \times 512 \times 768$  meshes

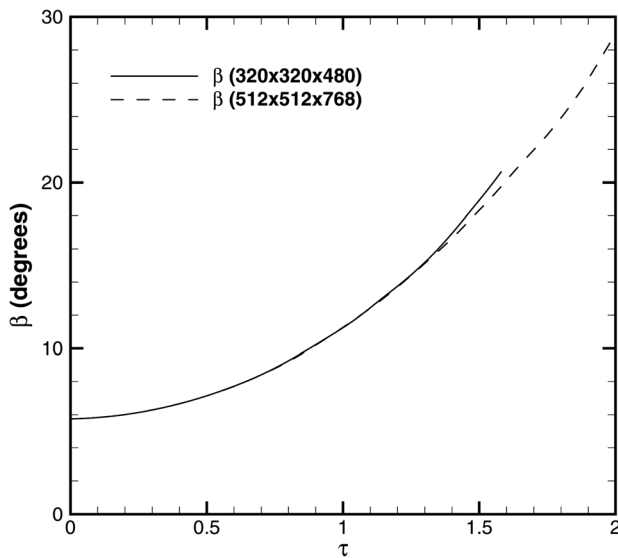


Fig. 15 RTI3D tilt-angle ( $\beta$ ) versus  $\tau$  for  $320 \times 320 \times 480$  and  $512 \times 512 \times 768$  meshes

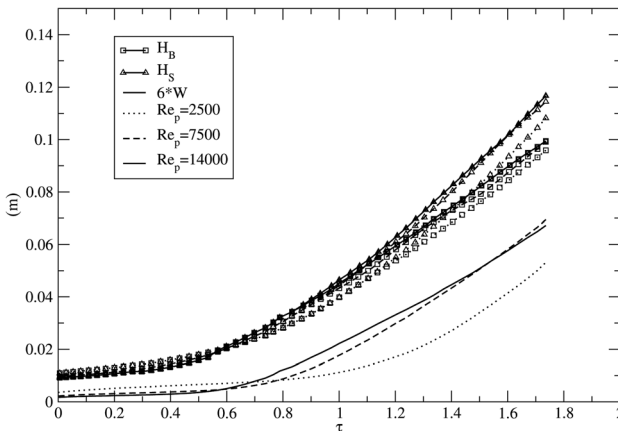


Fig. 16 CFDNS side wall bubble and spike heights and  $6 \times W$  at different  $Re_p$  values

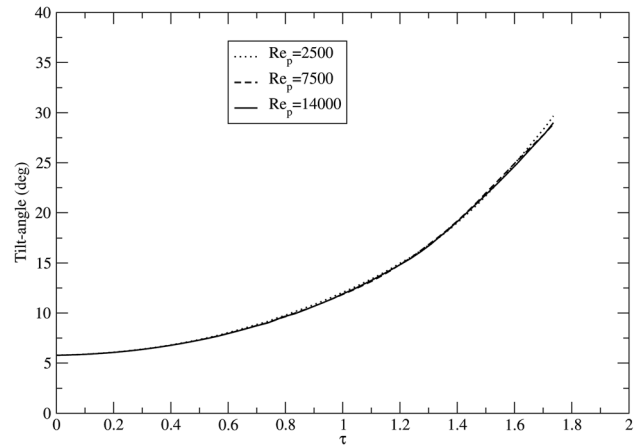


Fig. 17 CFDNS tilt-angle (degrees) at different  $Re_p$  values

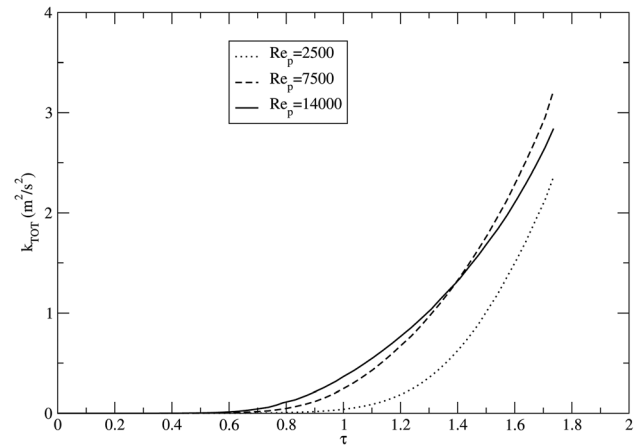


Fig. 18 Turbulent kinetic energy for the CFDNS cases

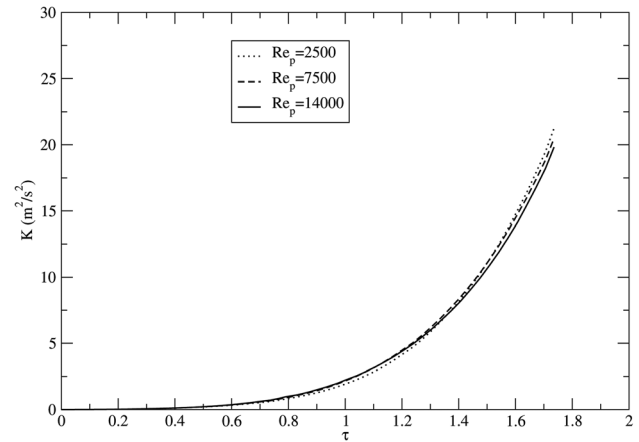


Fig. 19 Total kinetic energy for the CFDNS cases

on spike and bubble penetration (so the large-scale features are well resolved), and an increase in central mix width with a decrease in mesh resolution, which like TURMOIL, we attribute to early time reduced dissipation when the turbulence was poorly resolved. Although not shown here, the RTI3D contours for  $k$  compare well with those of TURMOIL. Instead Figs. 13(a) and 13(b) show the contours of “ $b$ ” for the fine and coarse mesh simulations respectively, where  $b$  may be viewed as an alternative molecular mix measure. However, comparison of the TURMOIL molecular mixing parameter  $\theta$ , in Figs. 11(a) and 11(b) in

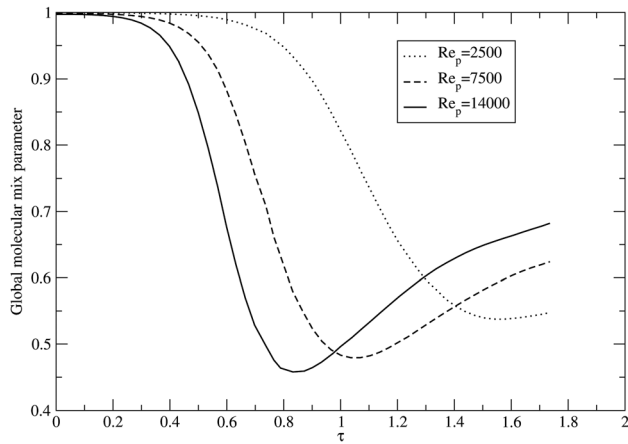


Fig. 20 Global mix parameter,  $\Theta$ , for the CFDNS cases

Fig. 13(a), is difficult because of the scale-range associated with each parameter, tending to miss the top of the range for the RTI3D results. But it is evident that the asymmetry apparent across the central mix region computed by TURMOIL is not readily apparent in Fig. 13, however care must be exercised because the parameters themselves are not directly comparable. Perhaps the most interesting observation from the comparison of TURMOIL and RTI3D simulations is the significant amount of molecular mixing that is apparently taking place, especially in regions of the bubble and spike.

Figure 14 shows the RTI3D spike and bubble penetrations that compare well with the TURMOIL ones of Fig. 9, reinforcing the qualitative agreement mentioned in the last paragraph. The rotation angle computed by RTI3D is given in Fig. 15, and

shows close agreement between the  $300 \times 300 \times 480$  and  $512 \times 512 \times 768$  meshes until relatively late-time, again indicating the two simulations capture the gross motions of the flow.

**4.3 Results from CFDNS.** DNS results are presented in Figs. 16–20 pertaining to the integral quantities specified above, and Figs. 21–24 pertaining to the 2D plots. The results show an expected convergence with respect to the Reynolds number. The tilt-angle, shown in Fig. 17, and total kinetic energy of Fig. 19, are close for the three cases, confirming the result above that the large overturning motion is relatively independent of the mixing. As expected, the wall bubble and spike heights of Fig. 16 increase as  $Re_p$  crosses the threshold for changing the growth behavior (Wei and Livescu [14]). Even larger differences are observed for the mix layer width in Fig. 16, and turbulent kinetic energy of Fig. 18, showing that the structure of the layer changes significantly with  $Re_p$ . Inspection of Fig. 20 reveals that the largest differences are obtained for the global molecular mixing parameter,  $\Theta$ . Unlike previous quantities, the results are still different between the  $Re_p = 7500$  and 14000 cases, and it is likely that a larger simulation is needed to see the asymptotic Re results. In the classical multimode Rayleigh-Taylor configuration, it is expected that the flow reaches asymptotic values of  $\Theta$  at long enough times, as the Reynolds number increases during the development of the instability, (Mueschke et al. [18]). At  $\tau = 1.741$ , for the  $Re_p = 14000$  case, the Reynolds number, based on the layer width,  $Re_h$  (see Mueschke et al. [18]) for the definition), is approx. 3700. This is a relatively large value, and the DNS results for  $\Theta$  reported here are consistent with previous experimental results at similar  $Re_h$  values (Mueschke et al. [18]), but it is likely not large enough to see the late time behavior. However, unlike the classical RT configuration, the time to reach the asymptotic  $\Theta$  behavior is also very important in the tilted RTI case, due to coupling with the overturning motion. This time depends on the  $Re_p$  value and the results

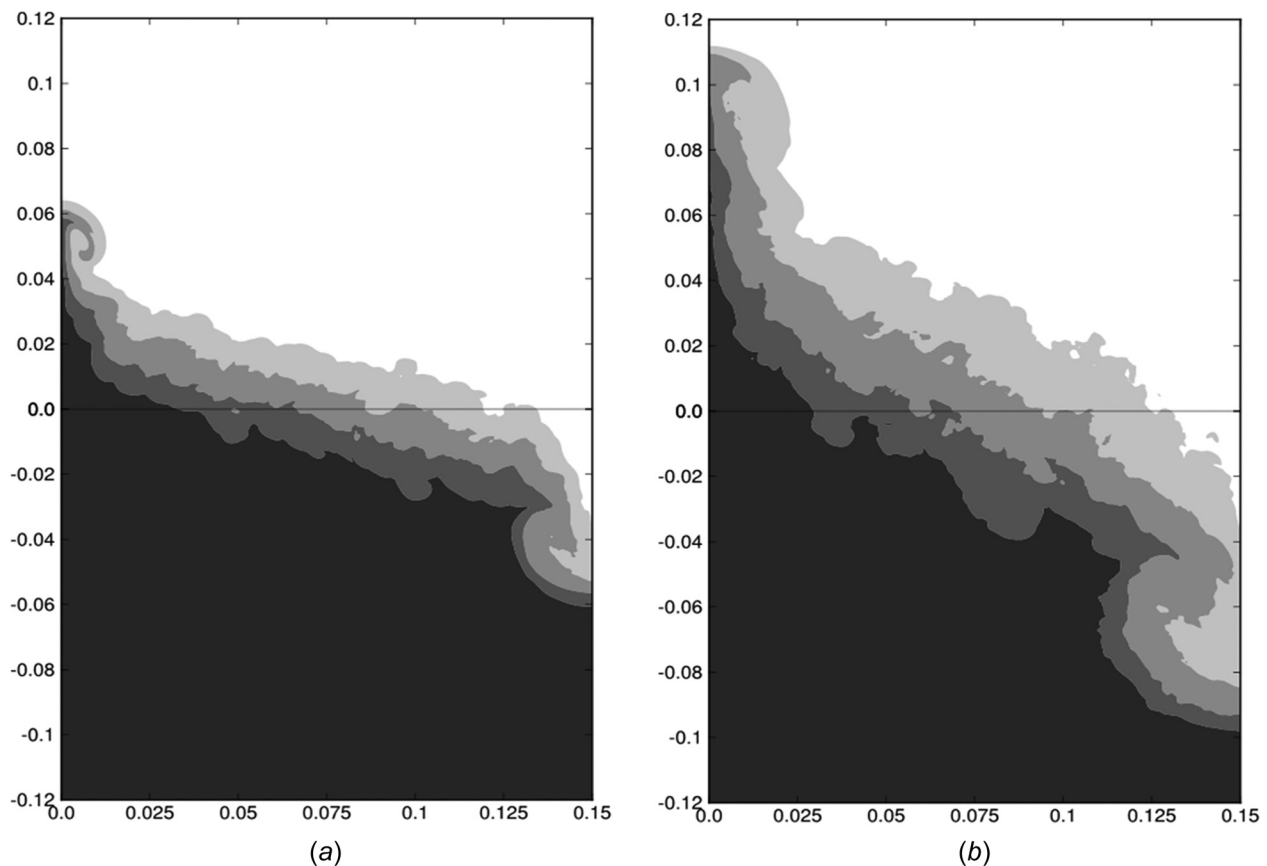


Fig. 21 CFDNS  $f_1$  contours at (a)  $\tau = 1.256$  and (b)  $t = 1.741$

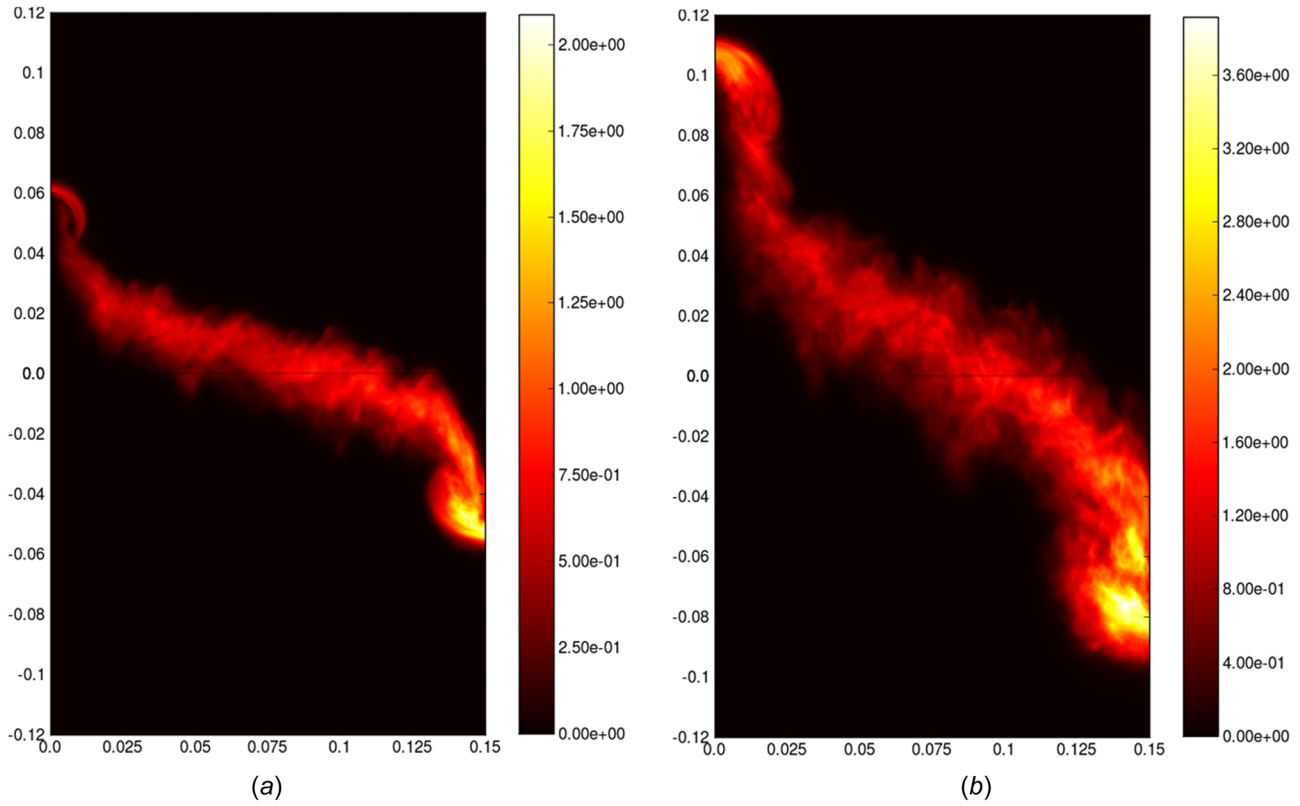


Fig. 22 CFDNS turbulent kinetic energy ( $m^2/s^2$ ) at (a)  $t = 1.256$  and (b)  $\tau = 1.741$

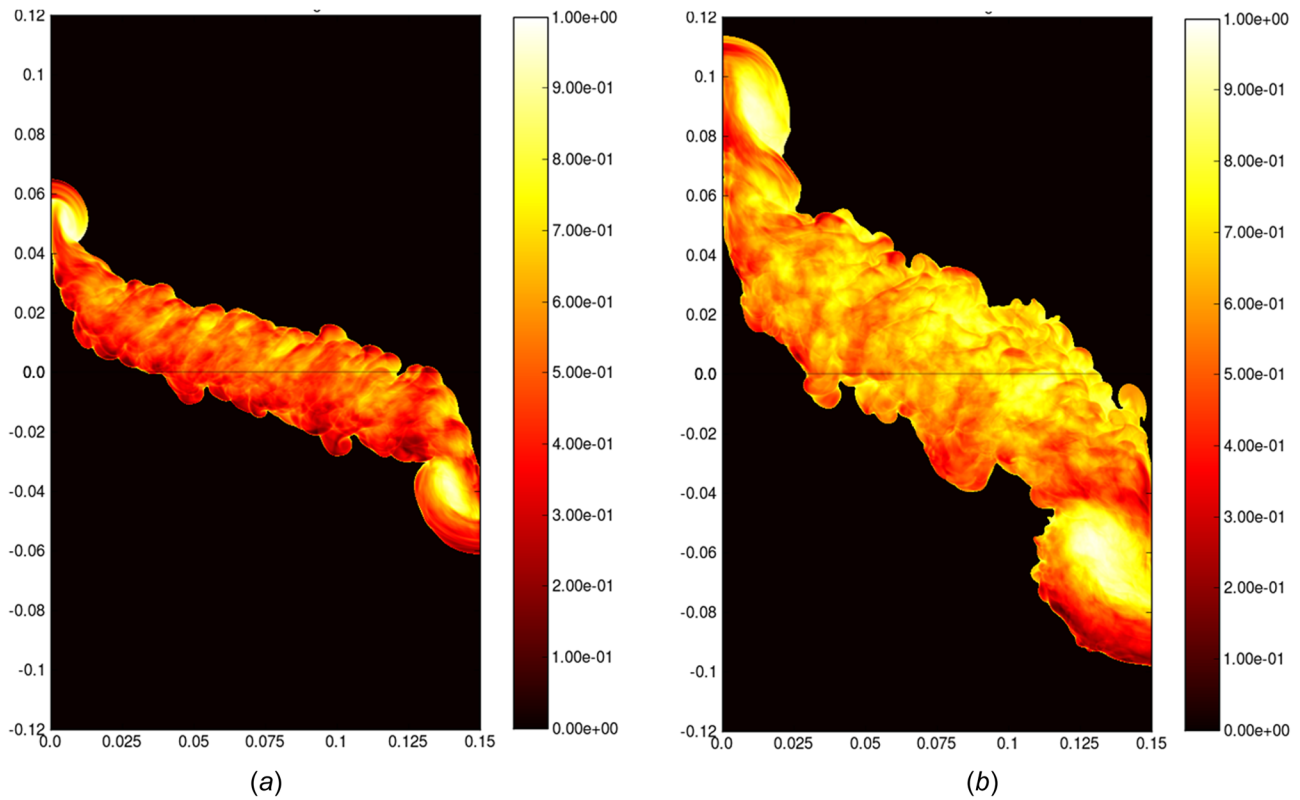


Fig. 23 CFDNS molecular mix parameter at (a)  $\tau = 1.256$  and (b)  $\tau = 1.741$

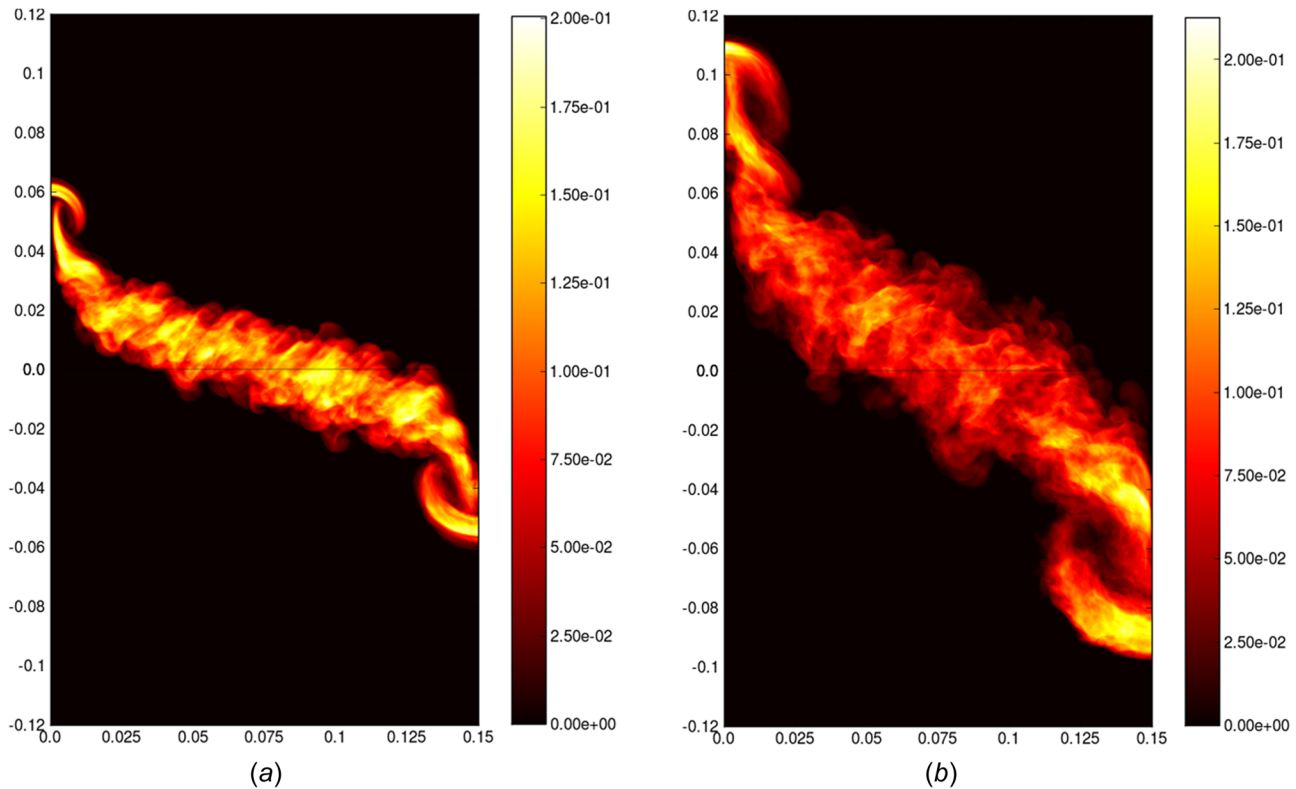


Fig. 24 CFDNS density specific volume correlation  $b$  at (a)  $\tau = 1.256$  and (b)  $\tau = 1.741$

highlight the importance of the Reynolds number for the tilted RTI problem. The 2D Figs. 21–24 showcase the wall bubble and spike, and the rich turbulence structure in the interior of the layer.

**4.4 Comparison of Results Between the Codes.** Sample results from the three codes have been shown. A detailed comparison of results is not presented in this paper, which focuses on the definition of the test problem. However, some key conclusions are worth noting, and the paper by Denissen et al. [19], in this special issue, discusses more results. The bubble and spike distances,  $H_b$  and  $H_s$ , the integral mix width  $W$ , and the volume fraction distributions are similar for the three methods. For ILES the effect of

mesh size is relatively small, and the DNS at the two highest Reynolds numbers give similar results to ILES. The global molecular mix parameter shows greater differences in behavior for the various methods, see Fig. 25. However, for ILES and the highest Reynolds number DNS the trends are similar. We also note that the initial values in Fig. 25 are high and, in particular, are close to unity for the DNS, which has a diffuse initial interface. The parameter then drops and finally rises as the “mixing transition” approaches. For ILES this transition is determined by numerical viscosity, and occurs earlier at lower resolution. However, all four ILES give a limiting value close to 0.75 at late time. For the highest Reynolds number DNS, the global molecular mixing parameter reaches 0.68 at  $\tau = 1.741$ . It seems likely that at higher Reynolds number the limiting value will be close to the ILES result.

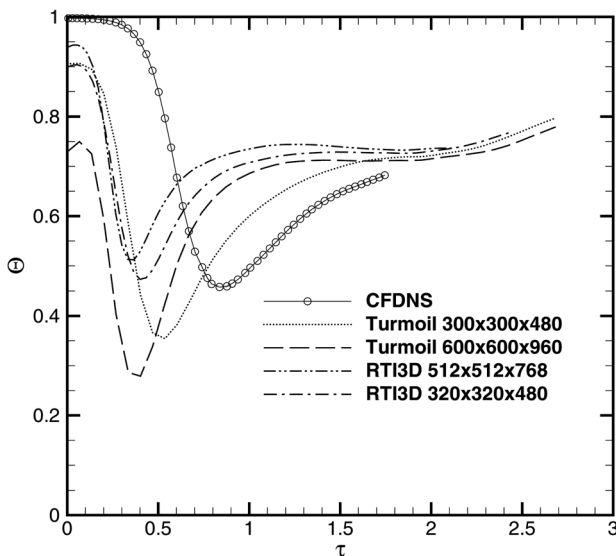


Fig. 25 Comparison of global molecular mixing with CFDNS  $Re_p = 14000$

## 5 Conclusions

The Tilted-Rig test problem is intended to serve as a validation problem for RANS models, and as such we have provided ILES and DNS simulations in support of the test problem definition. Moreover, comparison of simulations with experiment reveals that large-scale overturning can be well captured in all the simulations, similarly central mix widths, and spike/bubble sidewall penetrations are also in good agreement. Detailed comparison between the different simulation methodologies, ILES and DNS, reveals an overall good agreement between mix metrics such as the amount of molecular mixing. The DNS simulations reveal a dependency on Reynolds number that merits further experimental work. The generally good agreement between experiment, ILES, and DNS supports our assertion that the Tilted-Rig is a useful test problem to study 2D material mixing, and well-suited to validate 2D RANS model development.

## Nomenclature

$f_1, f_2$  = volume fractions of fluids 1 and 2  
 $g$  = tank acceleration

$H_s, H_b$  = left (spike) and right (bubble) plume penetration in the  $z$  direction (m)

$p$  = fluid pressure

$t$  = time

$u, v, w$  = fluid velocities in  $x, y$  and  $z$  directions (m/s)

$L_x, L_y, L_z$  = domain length in  $x, y$  and  $z$  direction (cm)

### Greek Symbols

$\beta$  = tilt-angle (degrees)

$\rho$  = fluid density

$\tau$  = nondimensional time defined in Eq. (7)

### Subscripts

1,2 = fluids 1 or 2

exp = experimental value

$b, s$  = bubble or spike

### References

- [1] Smeeton, V. S., and Youngs, D. L., 1987, "Experimental Investigation of Turbulent Mixing by Rayleigh-Taylor Instability III," AWE Report No. O 35/87.
- [2] Youngs, D. L., 1989, "Modeling Turbulent Mixing by Rayleigh-Taylor Instability," *Phys. D*, **3**, pp. 270–287.
- [3] Burrows, K. D., Smeeton, V. S., and Youngs, D. L., 1984, "Experimental Investigation of Turbulent Mixing by Rayleigh-Taylor Instability II," AWE Report No. O 22/84.
- [4] Read, K. I., and Youngs, D. L., 1984, "Experimental Investigation of Turbulent Mixing by Rayleigh-Taylor Instability," AWE Report No. O 11/83.
- [5] Andrews, M. J., 1986, "Turbulent Mixing by Rayleigh-Taylor Instability," Ph. D. thesis, London University, London.
- [6] Andrews, M. J., and Spalding, D. B., 1990, "A Simple Experiment to Investigate Two-Dimensional Mixing by Rayleigh-Taylor Instability," *Phys. Fluids*, **2**(6), pp. 922–927.
- [7] Dimonte, G., and Schneider, M., 2000, "Density Ratio Dependence of Rayleigh–Taylor Mixing for Sustained and Impulsive Acceleration Histories," *Phys. Fluids*, **12**(2), pp. 304–322.
- [8] Snider, D. M., and Andrews, M. J., 1994, "Rayleigh-Taylor and Shear Driven Mixing With an Unstable Thermal Stratification," *Phys. Fluids A*, **6**(10), pp. 3324–3334.
- [9] Youngs, D. L., 1994 "Numerical Simulation of Mixing by Rayleigh-Taylor and Richtmyer-Meshkov Instabilities," *Laser Particle Beam*, **12**, pp. 725–750.
- [10] Dimonte, G., Youngs, D. L., Dimits, A., Weber, S., Marinak, M., Calder, A. C., Fryxell, B., Biello, J., Dursi, L., MacNeice, P., Olson, K., Ricker, P., Rosner, R., Timmes, F., Tufo, H., Youns, Y.-N., Zingale, M., Wunsch, S., Garasi, C., Robinson, A., Ramaprabhu, and Nadreus, M. J., 2004, "A Comparative Study of the Turbulent Rayleigh-Taylor Instability Using High Resolution 3D Numerical Simulations: The Alpha Group Collaboration," *Phys. Fluids A*, **16**(5), pp. 1668–1693.
- [11] Livescu, D., Ristorcelli, J. R., Petersen, M. R., and Gore, R. A., 2010, "New Phenomena in Variable-Density Rayleigh-Taylor Turbulence," *Phys. Script.*, **142**, p. 014015.
- [12] Livescu, D., Wei, T., and Petersen, M. R., 2011, "Direct Numerical Simulations of Rayleigh-Taylor Instability," *J. Phys.*, **318**, p. 082007.
- [13] Livescu, D., and Ristorcelli, J. R., 2007, "Buoyancy-Driven Variable-Density Turbulence," *J. Fluid Mech.*, **591**, pp. 43–71.
- [14] Wei, T., and Livescu, D., 2012, "Late-Time Quadratic Growth in Single-Mode Rayleigh-Taylor Instability," *Phys. Rev. E*, **86**, p. 046405.
- [15] Holford, J. M., Dalziel, S. B., and Youngs, D. L., 2003, "Rayleigh-Taylor Instability at a Tilted Interface in Laboratory Experiments and Numerical Simulations," *Laser Particle Beam*, **21**(3), pp. 419–423.
- [16] Layzer, D., 1955, "On the Instability of Superposed Fluids in a Gravitational Field," *J. Astrophys.*, **122**.
- [17] Goncharov, V. N., 2002, "Analytical Model of Nonlinear, Single-Mode, Classical Rayleigh-Taylor Instability at Arbitrary Atwood Numbers," *Phys. Rev. Lett.*, **88**(13), p. 134502.
- [18] Mueschke, N. J., Schilling, O., Youngs, D. L., and Andrews, M. J., 2009, "Measurements of Molecular Mixing in a High-Schmidt-Number Rayleigh-Taylor Mixing Layer," *J. Fluid Mech.*, **632**, pp. 17–48.
- [19] Denissen, N., Rollin, B., Reiser, J., and Andrews, M. J., 2014, "The Tilted Rocket Rig: A Rayleigh-Taylor Test Case for RANS Models," *ASME J. Fluids Eng.*, (to be published).